1 The diurnal evolution of oceanic boundary layer beneath early-frozen
2 landfast ice in Prydz Bay, East Antarctica

3 Haihan Hu[1,2], Jiechen Zhao[3,4*], Petra Heil[5], Jingkai Ma[6], Fengming Hui[1,2*], Xiao Cheng[1,2]

4 [1]School of Geospatial Engineering and Science, Sun Yat-Sen University, Guangzhou 510275, China
5 [2]Southern Marine Science and Engineering Guangdong Laboratory, Zhuhai 519082, China
6 [3]Qingdao Innovation and Development Base (Centre) of Harbin Engineering University, Qingdao, 266500, China
7 [4]College of Underwater Acoustic Engineering, Harbin Engineering University, Harbin 150001, China
8 [5]Australia Antarctic Division & Australian Antarctic Programmer Partnership, Private Bag 80, Hobart TAS 7001, Australian
9 [6]Key Laboratory of Research on Marine Hazards Forecasting, National Marine Environmental Forecasting Centre, Beijing
10 100081, China

11 *Correspondence to*: Jiechen Zhao (zhaojiechen@hrbeu.edu.cn) and Fengming Hui (huifm@mail.sysu.edu.cn)

12 **Abstract.** The ice–ocean boundary layer parameters are one of the main drivers of sea ice mass balance in the Polar Regions.

13 To investigate the oceanic contribution to the landfast ice evolution, an integrated ocean observation system, including

14 Acoustic Doppler Velocimeter, COMPACT-CTD, and Sea Ice Mass Balance Array, was deployed near Zhongshan Station in

15 Prydz Bay, East Antarctica. The minute-resolution of ocean temperature, salinity, density, current, and heat flux from 16 to 23

16 April, 2021 were obtained and analysed. The results showed that ocean temperature experienced a jump increase, from -

17 1.59±0.03°C during 16–19 April to -1.47±0.07°C during 20–23 April, which may relate to the tide transform from semi-diurnal

18 to diurnal. Ocean salinity and density showed a gradual trend increasing by 0.013 psu day^{-1} and 0.009 kg m^{-3} day^{-1}, respectively,

19 related to the salt rejection of ice bottom freezing. The mean ocean velocity was 3.13±1.63 cm s^{-1} and 34% of the current

20 directions accounted to the northwest. Oceanic heat flux was estimated by the bulk parameterization method and residual

21 energy method, which were 32.26±18.07 W m^{-2} and 34.95±17.52 W m^{-2}, averaged for the study period respectively. Oceanic

22 heat flux showed a large increase during 20–23 April, which shut down ice growth and resulted in 2 cm melting at the ice

23 bottom. The high frequency of ocean observations allows us to deeply investigate diurnal changes of oceanic regimes and

24 understand their influences on sea ice evolution.

25 1 Introduction

26 In recent years, global warming has become more and more pronounced especially in the high latitudes (Manabe and Stouffer,

27 1980; Screen and Simmonds, 2010; Clem et al., 2020). Notably, the Antarctic region plays a pivotal role in driving and

28 modulating climate change on global scale (Massom and Stammerjohn, 2010). As a structural part of the polar ecosystem, sea

29 ice conditions reflect the polar ocean conditions and play a crucial role in the marine system and ecosystem structure. In

30 contrast to the rapid decline of Arctic sea ice since the late 1970s, Antarctic sea ice as a whole showed a slight trend of increase

31 up to recent years (Comiso et al., 2008; Liu and Curry, 2010). Antarctic sea ice extent peaked at above 20×10^6 km^2 in 2014,

32   but since has exhibited decreasing summer minima and winter maxima (Parkinson and DiGirolamo, 2021). Antarctic sea ice

33   extent has reached a new all-time low in 2021/22 (Raphael and Handcock, 2022; Wang et al., 2022), the causality for this

34   remains under discussion.

35

36   Fast ice is prevalent in Antarctic coastal areas, usually attached to the shorelines, ice shelves, glacier tongues, grounded

37   icebergs, or grounded shoals (Massom et al., 2001; Li et al., 2020). Compared with floating ice in the same region, the landfast

38   ice has a longer annual duration and generally is thicker, and its width can extend tens to hundreds of kilometres from the

39   shore. At the time of maximum winter sea ice extent in the Southern Hemisphere, the landfast ice area accounts for about 3–

40   4% of the total Antarctic sea ice area (Li et al., 2020), and the volume for about 14–20% of the entire Antarctic sea ice volume

41   (Fedotov et al., 2013). The proportion of landfast ice off East Antarctica exceeds that of other Antarctic regions (Giles et al.,

42   2008; Li et al., 2020). As a natural barrier between the ocean and the atmosphere, landfast ice strongly influences the interaction

43   between the air–ocean interface and the heat flux and water vapour exchange between the ocean and the atmosphere (Maykut

44   and Untersteiner, 1971; Heil et al., 1996; Heil, 2006). The formation of landfast ice mainly depends on the thermodynamic sea

45   ice growth. The existence and growth of landfast ice provide some of the essential functions for the Antarctic environment

46   such as providing a barrier to the glacial ice sheet (Massom and Stammerjohn, 2010; Miles et al., 2017) that otherwise would

47   be less constrained to calve and vanish into the Southern Ocean. Therefore, landfast ice is a crucial component in the Earth

48   system that cannot be ignored when assessing the role of Antarctica in the global climate system. Oceanic heat flux plays a

49   critical role in thermodynamic models of sea ice growth and is a crucial factor affecting the mass balance of sea ice. Parkinson

50   and Washington (1979) confirmed that seasonally varying oceanic heat flux impacts the annual sea ice growth. Understanding

51   changes in oceanic heat flux under ice plays a vital role in determining ice thickness and seasonal sea ice variations.

52

53   Oceanic heat flux can be estimated by measuring the temperature gradient, growth rate, and sea ice salinity (McPhee and

54   Untersteiner, 1982). Allison (1981) studied the landfast ice around Australia's Antarctica Mawson Station and found that the

55   oceanic heat flux showed a maximum value at the beginning of the sea ice growing season because the rapid growth of sea ice

56   established thermohaline convection and deepened the mixing layer by pumping warm water up. Heil et al. (1996) estimated

57   that mean annual oceanic heat flux at Australia's Antarctica Mawson Station ranged from 5 to 12 W m^{-2}. Lei et al. (2010)

58   studied the interannual variation of landfast ice in Prydz Bay during 2006 and pointed out that in the early stage of sea ice

59   growth, both the vertical temperature gradient of thin ice and the ice growth rate fluctuate strongly. Oceanic heat flux

60   estimations based on the flux balance equation at the ice–ocean interface varies from 7 to 18 W m^{-2} (based on 8 psu salinity),

61   with an oceanic heat flux of 11.8±3.5 W m^{-2} in April. Yang et al. (2016) calculated the oceanic heat flux in Prydz Bay by using

62   the HIGHTSI model with sea ice thickness measurements as input parameters. During the sea ice growing season (March–

63   November), the mean oceanic heat flux was 10 W m^{-2} and gradually decreased from the highest 25 W m^{-2} to 5 W m^{-2}. Zhao et

64   al. (2019) estimated the oceanic heat flux beneath sea ice in Prydz Bay using the residual energy method and found that the

65   oceanic heat flux ranged from 20.0 to 40.0 W m^{-2} during the early growth of landfast ice in Prydz Bay in 2011. In March, the

66   maximum monthly mean value was 33.8±7.5 W m^{-2}. While previous studies focused on seasonal variation and interannual

67   circulation of oceanic heat flux, there are few studies on short-term transient changes of oceanic heat flux in the early stage of

68   sea ice growth. McPhee et al. (1996) found that oceanic heat flux also changed significantly on the sub-diurnal scale with the

69   continuous flow of subglacial cold and warm ocean currents. Therefore, studying the effects of oceanic heat flux changes on

70   sea ice growth at the sub-diurnal scale is important.

71

72   Our study investigates the minute-resolution changes of oceanic heat flux beneath sea ice during the early growth season near

73   Zhongshan Station in Prydz Bay, East Antarctica. The motivation is to understand how oceanic heat flux affects the sea ice

74   growth in a diurnal scale, and to study the relationship between ocean temperature and current direction and their influence on

75   oceanic heat flux. We estimated oceanic heat flux using two different methods: (a) residual energy method based on modified

76   Stefan's Law; (b) a holistic parameterization approach using frictional velocities and the available heat content of frozen water.

77   Based on ocean temperature, salinity, and velocity observed by ADV, CTD, and SIMBA, the high time resolution changes of

78   oceanic heat flux were calculated and compared with previous studies. Section 2 describes field observations used in this study.

79   The results, including ocean temperature, salinity, density, and oceanic heat flux estimation are presented in Sect. 3. The

80   discussion is in Sect. 4, and conclusions are provided in Sect. 5.

81   **2 Observations**

82   Zhongshan Station (69°22′ S, 76°22′ E), the second Chinese Antarctic scientific research station, was established in February

83   1989 and operated year-round from then on. It is located in Prydz Bay, East Antarctica (Fig. 1a), and the surrounding near-

84   coastal ocean is covered by landfast ice from February to December. In the cold season, the extent of landfast ice may reach

85   up to 60–100 km north of Zhongshan Station. Typically, late every austral summer (i.e., late January), the landfast ice breaks

86   up due the mechanical forcing provided by wind stress, waves, and tide. The sea ice cover is then completely removed, with

87   exception of some small ice floes that may survive in narrow fjords and become second or multi-year sea ice in the subsequent

88   winter.

89

90   During 16 to 23 April 2021, an integrated ice–ocean interaction observation system was set up by the wintering team in the

91   coastal landfast ice about 1 km off Zhongshan Station (Fig. 1b). A cable-type CTD (model: ALEC ACTD-DF) was deployed

92   at 2 m beneath the ice surface and 30 m off the shoreline, where the water depth was 4.5 m. The measurement frequency was

93   both 30 s for the conductivity and temperature sensors. The accuracy was ±0.02 mS cm^{-1} (±0.03 psu) for conductivity (salinity)

94   and ±0.02°C for temperature. An Acoustic Doppler Velocimeter (model: SonTek Argonaut-ADV) was deployed 30 m north

95   of ACTD 5 m below the ice surface, where the water depth was 13.0 m. The frequency for velocity observations was 40 s, and

96   the sensor accuracy was ±0.001 m s^{-1}. A Sea Ice Mass Balance Array (model: SRSL SIMBA) was deployed 30 m north of

97   ADV, where the water depth was also 13.0 m. The SIMBA contained 240 temperature sensors mounted on the thermistor

98   string with 2 cm intervals to measure the vertical temperature profile across the air–snow–ice–ocean column every six hours,

99   at an accuracy of ±0.0625°C (Fig. 1c).

100

101   Snow depth and ice thickness were measured manually every five days around the integrated ice–ocean interaction observation

102   system. The records showed that snow and ice thickness was 0.045 m and 0.440 m on 16 April, while 0.020 m and 0.460 m

103   on 21 April 2021.
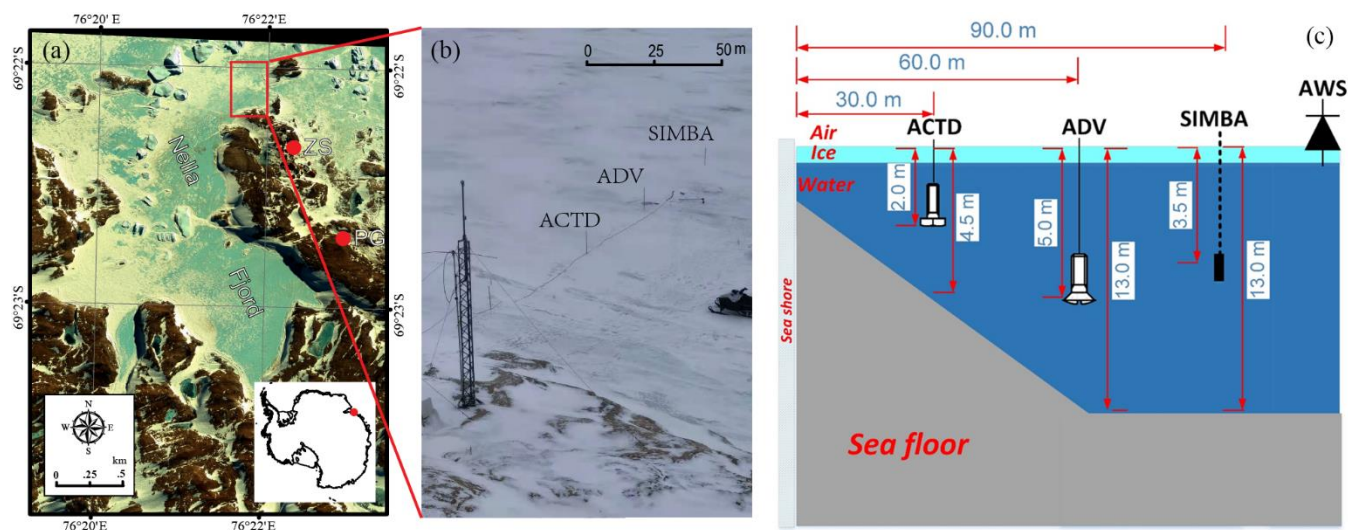
104

105   **Figure 1. (a) The map of the observation location in Nella Fjord near Zhongshan Station (the satellite image was modified from the**
106   **WorldView-2 multi-bands image taken on 20 Oct 2012); (b) The photo of the observation site taken on 12 April 2021 (the field**
107   **picture was taken by Jinkai Ma, one of the co-authors, during he worked as the wintering team member in Zhongshan Station); (c)**
108   **Schematic of the integrated ice–ocean interaction observation system off Zhongshan Station during austral winter 2021.**

109   **3 Results**

110   **3.1 Ice evolution**

111   The SIMBA temperature chains record the vertical temperature profiles at the atmosphere–ocean interface through the

112   atmosphere–snow–sea ice–ocean column. Numbering of thermistors starts at lowest of the temperature chain (in ocean). Figure

113   2a and 2b respectively show the vertical temperature profile and vertical temperature gradient of temperature data recorded by

114   the temperature chain. This is evident from Fig. 2a, the daily variation in air temperature (sensors 180–200) was significant,

115   with a maximum of 4.24°C between two adjacent days (in austral winter), and the air temperature was much lower than the

116   ice and ocean temperature during the study period. The sea ice temperature (sensor 155–180) showed a significant gradient,

117   varied between 0.11°C cm^{-1} and 0.24°C cm^{-1}. The ocean temperature (sensor 0–155) is maintained between -1.7°C and -1.9°C,

118   close to the freezing point. The difference in thermal conductivity between air, sea ice, and ocean results in distinct vertical

119   temperature gradients. The white dotted line showed the sea ice surface. The asterisk white solid line was the ice–water

120 interface which was determined by freezing point temperature as the threshold value. During the growth season, the ocean

121 temperature usually remains at freezing point, which is the reason for distinguishing sea ice with a large vertical gradient from

122 ocean with a basically constant temperature. It could be seen that the thickness of landfast ice showed an increase of about 2

123 cm from 16 to 21 April, consistent with the increase of landfast ice thickness from 0.44 to 0.46 m observed in the field.

124 However, after the 21 April, there was a decrease in the thickness of the landfast ice, with basal melt accounting for nearly 2

125 cm. The basal ice loss is likely in consequence of warming of the near-surface ocean due to increased oceanic heat flux at the

126 ice–water interface (detailed discussed later in Sect. 4.1).

127
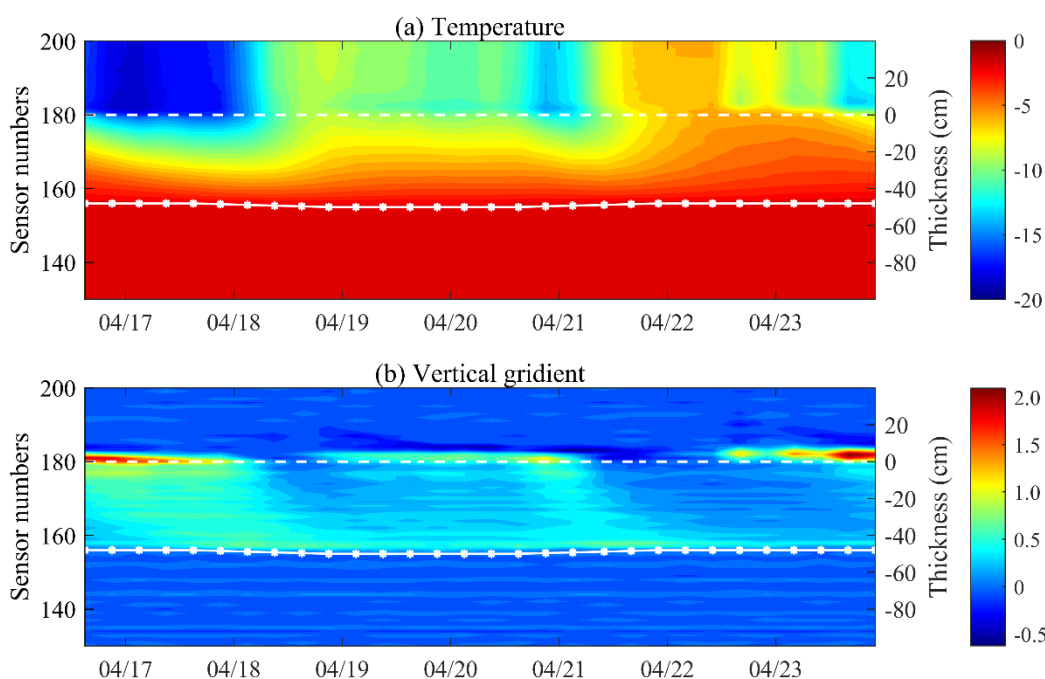
Figure 2. (a) Vertical temperature profiles; (b) Vertical temperature gradient. The asterisk white solid line and white dotted line in (a) and (b) are the ice bottom and ice surface, respectively.

3.2 Ocean temperature

131 The ocean temperature and salinity data were obtained from ACTD deployed approximately 2 m below the landfast ice surface.

132 The ACTD sampling rate was 30 s and recorded high-frequency temperature changes. During the study period, the ocean

133 beneath ice was relatively warm, with an average temperature of about -1.53±0.08℃, while the average temperature at the

134 bottom of the sea ice (about 0.1 m above ice bottom) was about -3.12±0.71℃. As a result, the heat transferred from warm

135 water to cold sea ice inhibited ice bottom growth, and counteracted to the effect of the cold atmosphere on the ice surface. The

136 ocean temperature exhibited a jump increase after 20 April (Fig. 3). The ocean temperature from 16 to 19 April remained

137 relatively stable, with an average temperature of -1.59±0.03℃, while increased significantly from 20 to 23 April, with an

average temperature of -1.47±0.07°C. The ocean temperature showed an obvious diurnal signal, the largest daily deviation

was 0.35°C on 21 April and the smallest one was 0.12°C on 18 April. Warmer temperatures allowed more heat flux to be

transferred from the water to the sea ice base, balancing the conductive heat flux and inhibiting sea ice growth, consistent with

the ice basal melt of 2 cm observed by SIMBA (Sect. 3.1).
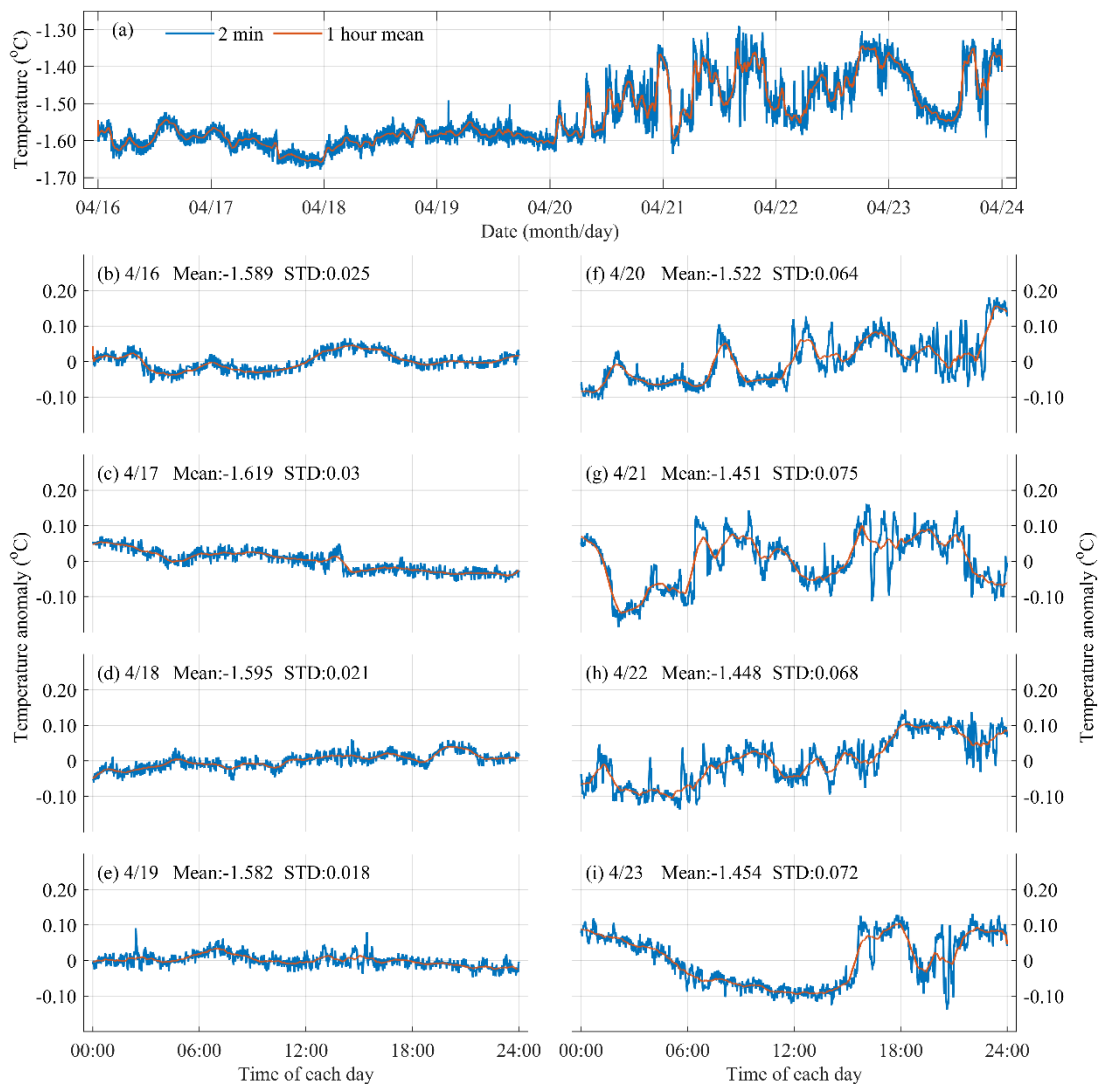
Figure 3. (a) The ocean temperature observed by ACTD at 2 m beneath the landfast ice surface from 16 to 23 April. (b–i) The diurnal anomalies based on the according daily mean. The blue and red lines represented the 2 minutes and 1 hour interval data records, respectively.

3.3 Ocean salinity

Compared with the change of ocean temperature, ocean salinity was relative stable (Fig. 4). The largest daily deviation was 0.14 psu on 16 April and the smallest was 0.66 psu on 17 April. During the study, the ocean salinity remained at 33.35±0.03 psu, and the mean upward trend was fast (0.017 psu day^{-1}) during 16 to 19 April and then slow (0.003 psu day^{-1}) from 20 to 23 April, which might be related to the slowdown of the growth of sea ice in the following days due to the increase of the ocean temperature. The temperature rise shut down the ice bottom freezing, then slowed down the salt rejection of sea ice.
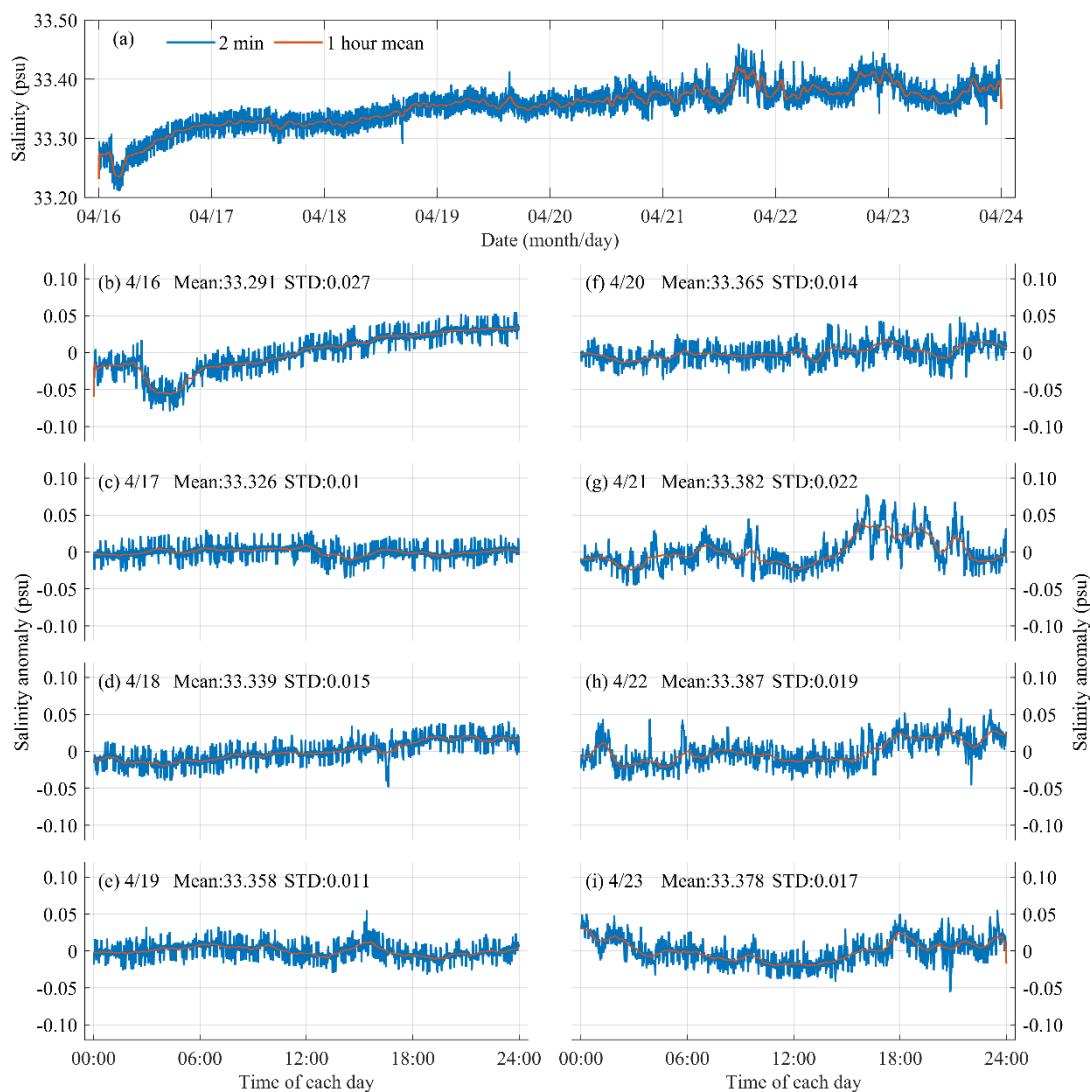
Figure 4. (a) The ocean salinity observed by ACTD at 2 m beneath the landfast ice surface from 16 to 23 April. (b–i) represent the diurnal anomalies based on the according daily mean. The blue and red lines represented the 2 minutes and 1 hour interval data records, respectively.

3.4 Ocean density

The ocean density is a function of temperature and salinity. Millero and Poisson (1981) proposed an internationally recognized atmospheric equation for the state of ocean, which is calculated as follows:

$$\rho - \rho_0 = AS + BS^{3/2} + CS^2 \tag{1}$$

Where, ρ and ρ_0 are functions of temperature (°C) and salinity, the coefficients for the combined data are:

$$A = 8.24493 \times 10^{-1} - 4.0899 \times 10^{-3}t + 7.6438 \times 10^{-5}t^2 - 8.2467 \times 10^{-7}t^3 + 5.3875 \times 10^{-9}t^4 \tag{2}$$

$$B = -5.72466 \times 10^{-3} + 1.0227 \times 10^{-4}t - 1.6546 \times 10^{-6}t^2 \tag{3}$$

$$C = 4.8314 \times 10^{-4} \tag{4}$$

The absolute densities could be calculated using the value for pure water from (Bigg, 1967):

$$\rho_0(kg \cdot m^{-3}) = 999.842594 + 6.793952 \times 10^{-2}t - 9.095290 \times 10^{-3}t^2 + 1.001685 \times 10^{-4}t^3$$

$$-1.120083 \times 10^{-6}t^4 + 6.536332 \times 10^{-9}t^5 \tag{5}$$

Combining the salinity equation above with the ocean temperature and salinity measured by ACTD, it is convenient to calculate the change of ocean density under landfast ice. The ocean density exhibits an overall increasing trend during the study from 16 to 23 April (Fig. 5). During the study, the average density of the mixed layer was 1026.84±0.02 kg m⁻³, and the mean increasing trend was fast (0.011 kg m⁻³ day⁻¹) during 16 to 19 April with an average density of 1026.82±0.02 kg m⁻³, and then slow (0.003 kg m⁻³ day⁻¹) from 20 to 23 April, but the daily density variation was also severe, with an average density of 1026.86±0.01 kg m⁻³. The largest daily deviation was 0.11 kg m⁻³ on 16 April and the smallest one was 0.05 kg m⁻³ on 17 April.
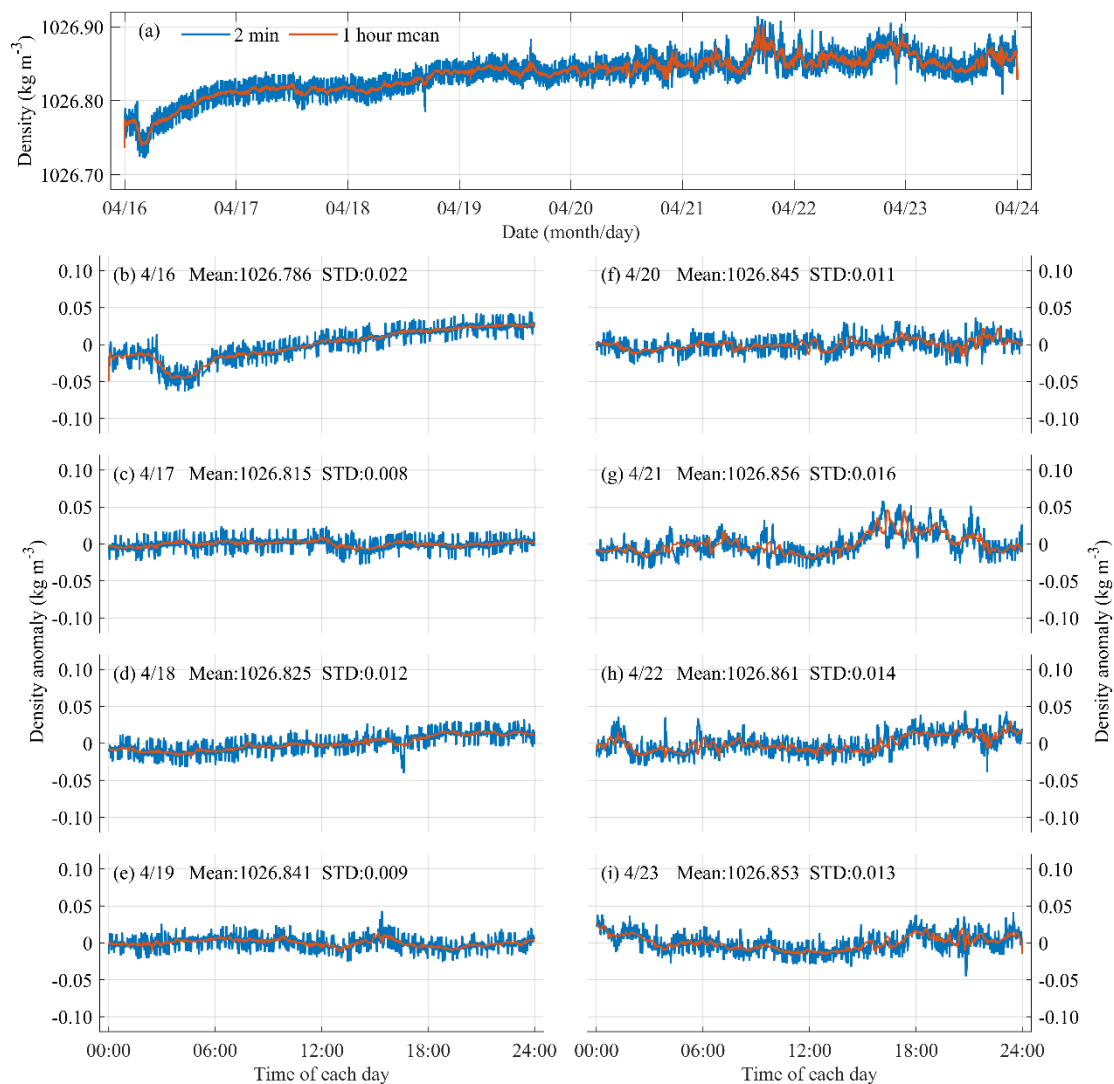
Figure 5. (a) The ocean density calculated by the temperature and salinity observed by ACTD at 2 m beneath the landfast ice surface from 16 to 23 April. (b–i) represent the diurnal anomalies based on the according daily mean. The blue and red lines represented the 2 minutes and 1 hour interval data records, respectively.

3.5 Ocean current

The current velocity beneath the landfast ice was obtained from ADV about 5 m below the ice surface. Figure 6 showed the velocity of due north (V), due east (U), and the vector sum of U and V. It can be seen from the figure that, the current velocity was relatively stable and showed periodic oscillation, with an average speed of about 3 cm s^{-1} and a maximum of about 10 cm s^{-1}. Combined with the ROSE analysis of the current direction (Fig. 7), the domain direction of the current outside Zhongshan Station is mainly northwest (300°–330°).

184

185 The daily ocean current direction showed a periodic change under the influence of the tide. In general, the current in this area

186 was mainly compound current and northwest offshore current. Fig. 8 showed the daily current and water level anomaly from

187 16 to 23 April. The water level anomaly for Zhongshan Station was obtained from the Bureau of Meteorology, Australia. The

188 direction of the ocean current around Zhongshan station was alternating under the action of tide, mainly the offshore current

189 in the northwest direction (315°). From 16 to 19 April, the ocean current indicated a semi-diurnal tides condition. From 9:00

190 to 15:00 and from 21:00 to 3:00 of the next day, it was mainly the offshore flow in the northwest direction (315°), along with

191 the water level anomaly gradually decreased. From 3:00 to 9:00 and from 15:00 to 21:00, it was mainly the onshore flow in

192 the southeast direction (135°), and the water level anomaly increased gradually. However, from 20 to 23 April, the onshore

193 flow gradually decreased, and the offshore flow gradually increased, indicated a change from semi-diurnal tide to full diurnal

194 tide. The change of tide condition weakened the vertical mixing, led to relative warm water existing under the landfast ice, and

195 then affected the oceanic heat flux (detailed discussed later in Sect. 4.1).
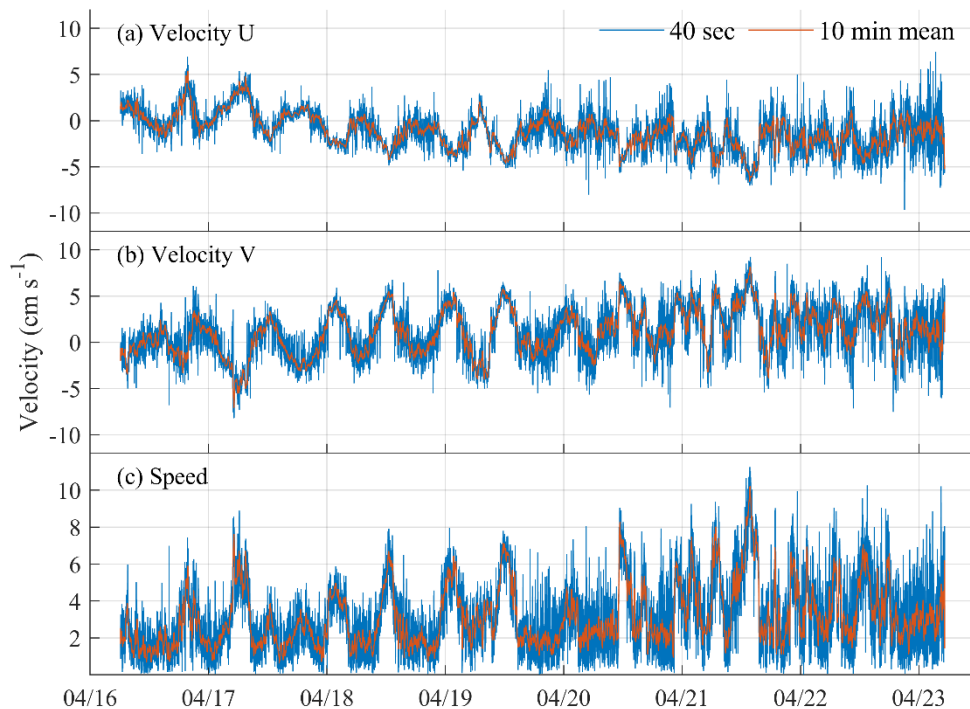
196

197 **Figure 6. The time series of current velocity beneath the landfast ice observed by ADV from 16 to 23 April. (a) U; (b) V; (c) Speed.**
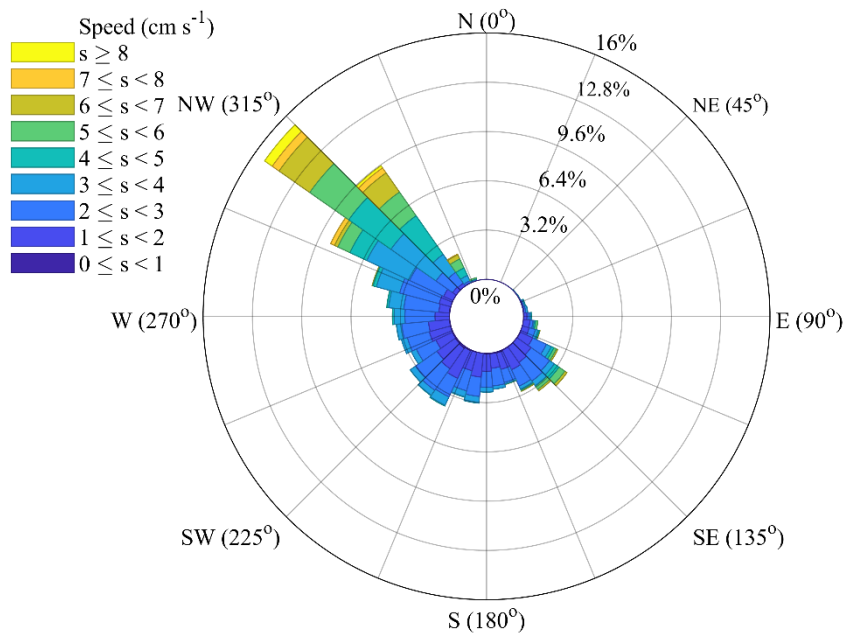
198

199   **Figure 7. The rose diagram of ocean current direction beneath the landfast ice observed by ADV from 16 to 23 April.**
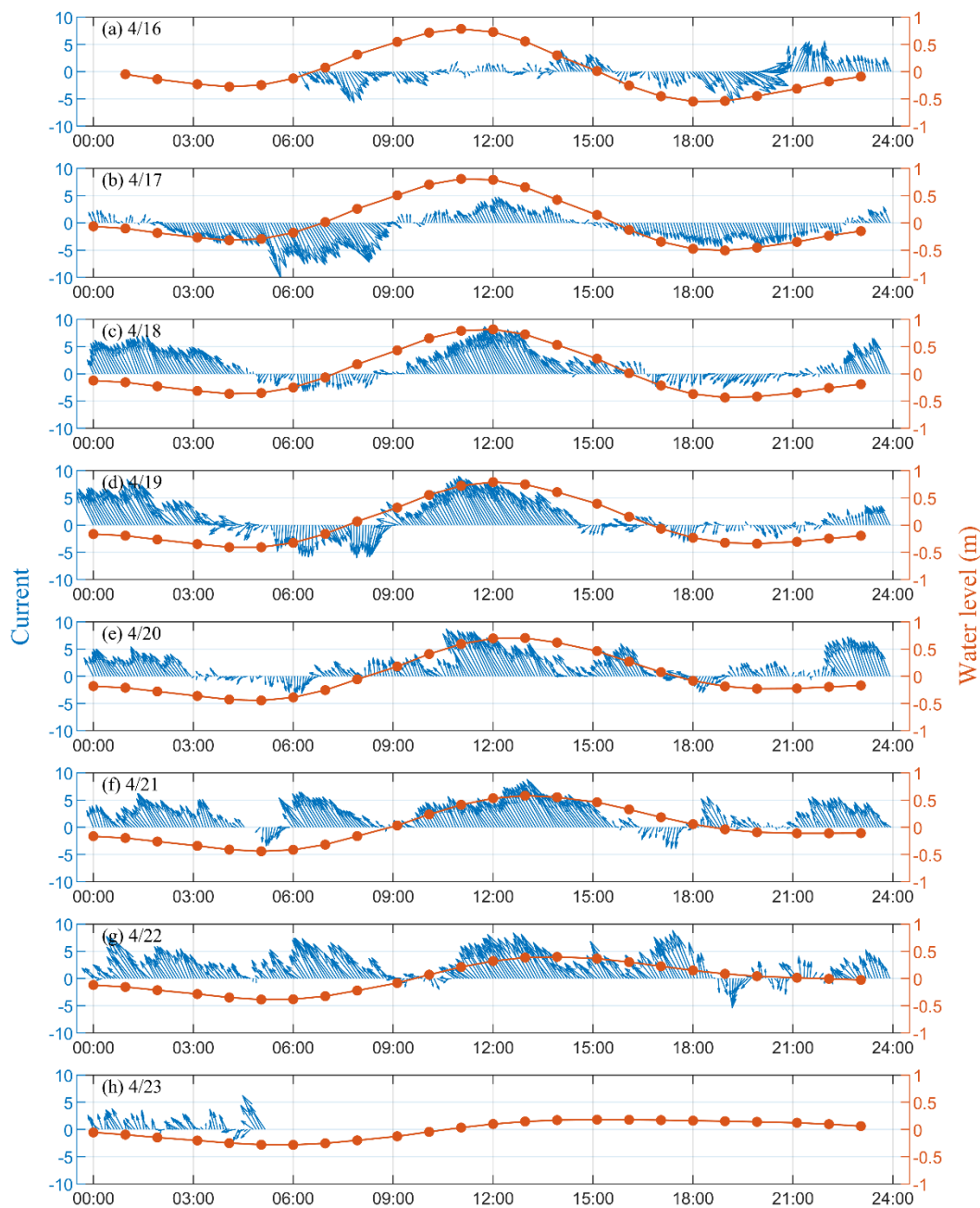
Figure 8. Daily illustration of 2 min current and hourly water level anomaly from 16 to 23 April. The blue vector arrow indicated the 2 min direction and velocity of the ocean current observed by ADV; the solid red line indicates the hourly water level anomaly obtained from BoM, Australia.

3.6 Oceanic heat flux

3.6.1 Residual energy method

The heat balance between ocean and atmosphere influenced the growth and melting of sea ice. During this study, mean air temperature from 16 to 23 April was about -10°C, which provided a large upward conductive heat flux and contributed to the ice bottom growth. At the same time, the relative warmer ocean (mean -1.53±0.08°C) provided an upward heat flux to sea ice and slowed down the bottom freezing processes. Determining the heat balance between atmosphere–ice–ocean is critical for studying sea ice mass balance. At the bottom of the sea ice, the heat balance could be expressed by an equilibrium equation as follow, and this equation could be used to estimate the residual oceanic heat flux (McPhee and Untersteiner, 1982; Perovich and Elder, 2002; Lei et al., 2014):

$$F_w = F_c + F_l + F_s \qquad (6)$$

Where F_w is the heat flux from the ocean to the sea ice, F_c is the heat conduction flux in the sea ice, F_l is the latent heat flux caused by the freezing or melting of the sea ice, and F_s is the specific heat flux generated by the temperature change in the ice. In the formula, the signs of melting, heating, and upward heat flow are positive, while the signs of cooling, freezing, and downward heat flow are negative.

The following equation solved the conductive heat flux:

$$F_c = k_i \frac{T_0 - T_f}{H} \qquad (7)$$

Where k_i is the thermal conductivity of sea ice, which is a function of temperature and ice salinity (Untersteiner, 1961); T_0 is sea ice temperature at the reference layer; H is sea ice thickness; T_f is the freezing point temperature of ocean, which is a function of salinity (Millero, 1978). The freezing point temperature was estimated as:

$$-T_f = 0.0575 S_w - 1.710523 \times 10^{-3} S_w^{3/2} + 2.154996 \times 10^{-4} S_w^2 \qquad (8)$$

Where S_w is the salinity of mixed layer water, the calculation of latent heat flux and specific heat flux could be solved by the following equation (Semtner, 1976; Lei et al., 2014):

$$F_l = -\rho_i L_i \frac{dH}{dt} \qquad (9)$$

$$F_s = \rho_i c_i \Delta H \frac{dT}{dt} \qquad (10)$$

Where ρ_i is the density of the bottom sea ice; L_i is the latent heat of freezing sea ice; c_i is the specific heat capacity of sea ice; dH is the sea ice thickness of the reference layer; dH/dt is the growth rate of sea ice; dT/dt is the temporal gradient of reference sea ice temperature; Where L_f and c_i are functions of sea ice salinity and temperature. Lei et al. (2010) pointed out that the average annual density of landfast ice in Prydz Bay is 910 kg m^{-3}, and the density of ice under ocean ranges from 893 to 948 kg m^{-3}, and the average annual salinity is 4 psu. Considering that the research period of this study was the early growth of landfast ice and the high salinity in ice, the landfast ice density adopted in this study was 940 kg m^{-3}, and the saltiness was 5

psu. So, the following formula could be used to calculate the thermal conductivity, latent and specific heat of sea ice at different temperatures (Untersteiner, 1961; McPhee and Untersteiner, 1982; Lei et al., 2010):

$$k_i = k_0 + 0.13\frac{S_i}{T_i} \tag{11}$$

$$L_i = \left[1 - S_i - \frac{S_i}{S_w}(1 - S_w)\right]L_f \tag{12}$$

$$c_s = -\frac{S_i \alpha T_i^2}{L_i} + \frac{S_i}{\alpha T_i}(c_w - c_{pi}) + c_{pi} \tag{13}$$

Where k_0 thermal conductivity of sea ice (2.03 W m^{-1} °C^{-1})); S_i is the salinity of sea ice; S_w is mixed layer salinity; L_f is the latent heat of pure ice (333.4 kJ kg^{-1}); T_i is the reference sea ice temperature; c_w is the specific heat capacity of water (4.23 kJ kg^{-1} °C^{-1}); c_{pi} is the specific heat capacity of pure ice (2.01 kJ kg^{-1} °C^{-1}); α = -0.0182°C^{-1} is a constant of ice salinity.

Generally speaking, the temperature of the sea ice varies significantly due to atmospheric and ocean temperature, and the vertical temperature profile of sea ice was approximately linear in the cold season. Therefore, an appropriate reference layer was used to calculate the vertical temperature gradient in Eq. (7). Usually, previous studies selected a certain distance from the ice bottom as the reference level. McPhee and Untersteiner (1982) set the reference level of 0.50–0.90 m thick ice to 0.50 m away from the ice surface. Perovich and Elder (2002) developed the reference level of ice with a thickness of 2.13–2.58 m at 1.75 m away from the ice surface. Lei et al. (2014) set the reference layer at 0.40–0.70 m above the ice base. Ice thickness in this study was around 0.4 m, 0.2 m above the ice bottom was taken as the reference level in this study, and the vertical temperature gradient in F_c was calculated by the temperatures at 0.2 m and the ice bottom. F_s represents the temporal change of heat content in sea ice inside this reference layer, and F_l is the growth or melting of the sea ice bottom.

During the study period, the freezing point temperature estimated by Eq. (8) gradually decreased and reached the lowest value -1.83°C on 21 April, along with the evolution of ocean salinity beneath sea ice. Figure 9 shows the heat fluxes in the energy balance equation. During the study period, air temperature showed a diurnal cycle and inflected by a warm event (Fig. 2a). The conductive heat flux (F_c) showed a response to the air temperature variation and had a certain lag.

The variation of the latent heat flux (F_l) was strongly correlated with the growth and ablation of sea ice. From 16 to 20 April, sea ice bottom was freezing, F_l was positive. From 21 to 24 April, due to the influence of warm and robust ocean current, a small amount of melting occurred at the ice bottom and F_l was negative. F_s was relative smaller throughout the investigation period, varying around 0. The estimated 6 hour oceanic heat flux showed a significant increase before 21 April and then decline. The average oceanic heat flux was 23.40±5.35 W m^{-2} during 16–19 April, and 45.06±18.30 W m^{-2} during 20–23 April. The average of oceanic heat flux during the whole study period was 34.95±17.52 W m^{-2}. The average daily oceanic heat flux reached the maximum 66.51±2.96 W m^{-2} on 21 April, according to a bottom melting (about 2 cm) at the bottom of sea ice.
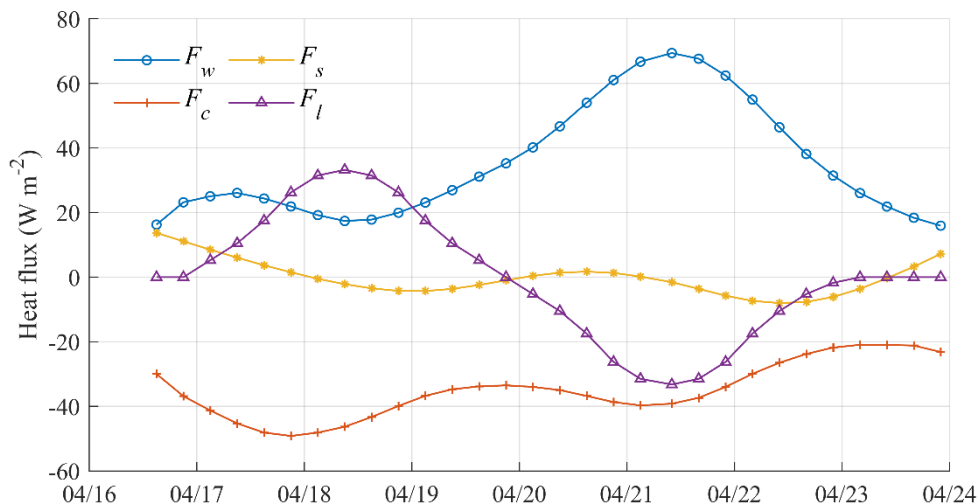
Figure 9. Estimated 6 hour conductive heat flux (F_c), latent heat flux (F_l), specific heat flux (F_s) and oceanic heat flux (F_w) by the residual energy method during 16 April to 23 April, 2021.

3.6.2 Bulk parameterization method

This section will consider measurements of current, temperature, and salinity in the upper ocean mixed layer beneath ice cover to evaluate the turbulent heat flux at the ice–ocean interface by the parameterized method.

Sea ice provides a rigid constraint on heat flow in the upper ocean boundary layer at the ice–ocean interface, where the temperature is close to freezing point in the growth season. The heat flux F_w from the mixed layer at the bottom of the sea ice could be calculated by the following formula (Guo et al., 2015):

$$F_w = \rho_w c_w \langle w'T' \rangle \tag{14}$$

Where ρ_w is the density of the ocean in the mixed layer, c_w is the specific heat capacity of ocean (3980 kJ kg^{-1} °C^{-1}); $\langle w'T' \rangle$ is the turbulent heat flux. The heat transfer from the mixed layer to the sea ice depends on both the turbulent stress at the ice–ocean interface (characterized by frictional velocity u_0^* as the square root of the kinetic stress at the interface) and the effective heat content of the fluid in the turbulent boundary layer, which is roughly proportional to the height of the mixing layer temperature above freezing point (McPhee, 1992; McPhee et al., 1999; Kirillov et al., 2015). The turbulent heat flux could be parameterized as:

$$\langle w'T' \rangle = c_H u_0^* \Delta T \tag{15}$$

Where c_H represents the Stanton number of heat exchange efficiency, is the difference between the mixed layer temperature and its freezing point temperature, u_0^* is the friction velocity at the interface. For the bottom boundary layer of sea ice, the exchange coefficient has been shown to be almost constant, $c_H = 0.0057$ (McPhee, 2002). Therefore, Eq. (14) could be expressed as:

288
$$F_w = \rho_w c_w c_H u_0^* \Delta T \tag{16}$$

289 Due to the lack of a velocity profile or roughness of the bottom boundary layer of sea ice, it is usually assumed by the law of

290 quadratic resistance to be related to free-stream current beyond the boundary layer, i.e., the friction velocity uses a statistical

291 relationship to determine u_0^* from the square root of the kinematic ice–ocean stress (τ) (McPhee, 1979):

292
$$u_0^2 = \sqrt{\tau} \tag{17}$$

293
$$\tau = 0.0104 V^{1.78} \tag{18}$$

294 Where, V is absolute flow velocity relative to stationary landfast ice, recorded from ADV (about 5 m below the ice surface).

295 During the study period, the freezing point temperature of ocean decreased gradually along the increase of ocean salinity, and

296 the height of ocean temperature higher than freezing point (ΔT) increased gradually, with a mean of 0.29±0.08℃. From 16 to

297 19 April, the average ΔT was 0.27±0.02℃. With the jump increase of ocean temperature, the average ΔT increased to 0.36±0.07℃

298 during 20–23 April.

299

300 The daily range of oceanic heat flux calculated was 18.02–53.70 W m^{-2} for bulk parameterization method, and 19.72–66.51

301 W m^{-2} for the residual energy method (Fig. 10a). According to bulk parameterization method, mean oceanic heat flux was

302 32.26±18.07 W m^{-2} from 16 to 23 April, of which it was 21.71±10.08 W m^{-2} from 16 to 19 April, and was 44.64±17.50 W m^{-2}

303 from 20 to 23 April. The detailed were shown in the Table 1.

304

305 According to the average daily oceanic heat flux calculated by the two methods shown in Fig. 10b, it can be seen that the two

306 methods produced similar diurnal variations of oceanic heat flux during the study period, which were relatively small before

307 April 20 and increased significantly thereafter. However, the variance of daily oceanic heat flux was significantly different

308 between the two methods. Compared with the residual energy method, the daily variance of bulk parameterization method was

309 larger, which could reflect the instantaneous change of oceanic heat flux due to the observation data with high sampling

310 frequency.

311

312 The results of oceanic heat flux indicated that the significant increase of ocean temperature in the mixed layer beneath the

313 landfast ice on 20 April caused a significant increase of oceanic heat flux. A large amount of heat was transferred to the sea

314 ice through ocean since 21 April, contributed to the basal sea ice melt (about 2 cm) observed by SIMBA. The minute-resolution

315 observations of ocean temperature, salinity, density, and velocity beneath landfast ice measured by ADV and ACTD provided

316 a good chance to investigate the rapid and detailed changes of oceanic heat flux, which effectively impact the growth of sea

317 ice.
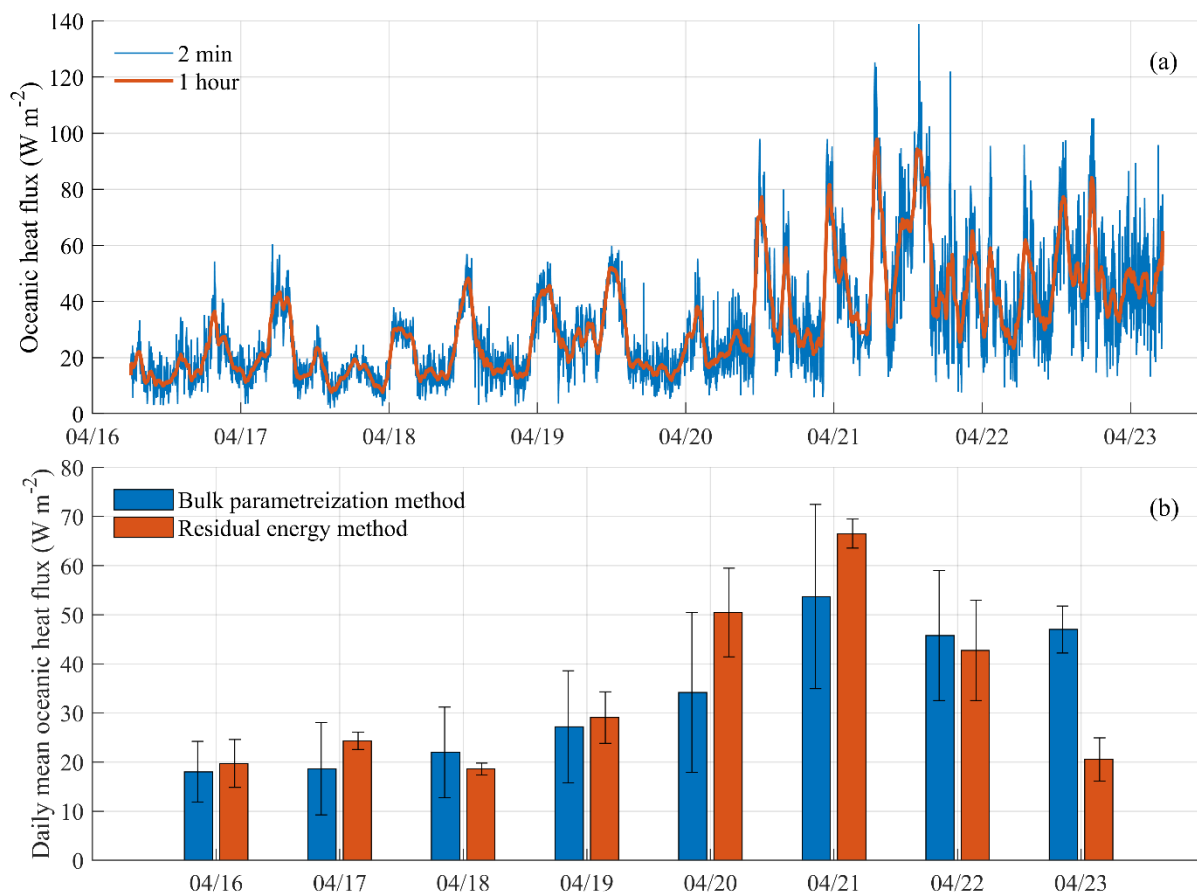
Figure 10. (a) High resolution oceanic heat flux calculated by bulk parameterization method, the blue and red lines represented 2 min and 1 hour results, respectively; (b) Daily mean oceanic heat flux calculated by two different methods: Bulk parameterization method and Residual energy method.

Table 1. Inter-comparisons of mean oceanic heat flux of two methods for calculating oceanic heat flux (W m^{-2})

Methods	16–19 April	20–23 April	Totally
Residual energy method	23.40±5.35	45.06±18.30	34.95±17.52
Bulk parameterization method	21.71±10.08	44.64±17.50	32.26±18.07

4. Discussions

4.1 The potential influences of tide on oceanic heat flux

The current observations from ADV indicated a diurnal back and forth movements under the landfast ice in the influences of tides, and further analysis suggested a dominated direction of northwest (34% of total records). The water level products of BoM showed that, water level amplitude experienced a decrease from around 1.8 m on 16 April to around 0.5 m on 23 April (Fig. 11), which indicates that the tides became weaker and the vertical mixing induced by the tides would decrease a bit.
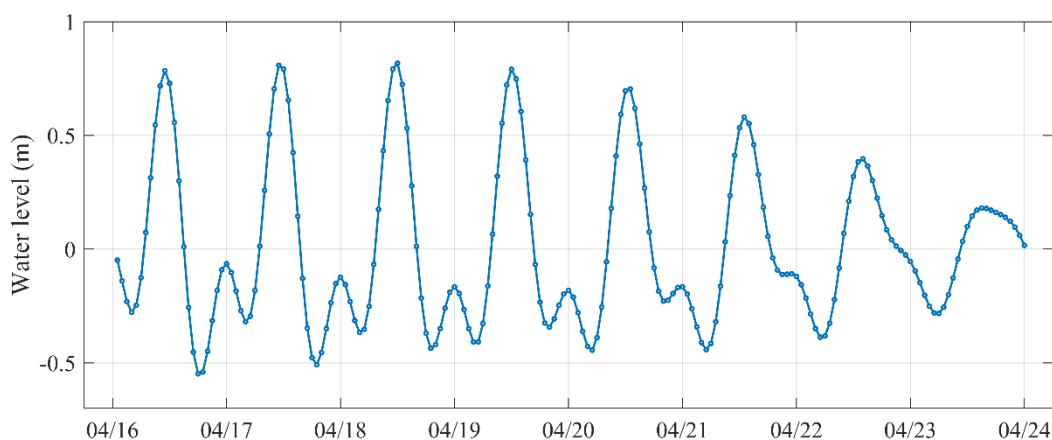
Figure 11. Hourly water level merged by BoM product and harmonic constant calculation during 16 to 23 April

The comparisons between current direction and temperature measured by ADV at 5 m beneath ice surface clearly showed that mean temperature for the southeast current (120–150°) was the lowest, which was -1.80±0.11°C. The average temperature for the offshore current in the northwest direction (300–330°) was the highest, at -1.67±0.13°C (Fig. 12a). Those results indicated that currents from outer open water carried the colder water to the coast, causing the ocean temperature beneath the landfast ice decrease.

Figure 12b showed the ocean temperature and salinity evolution observed by ACTD located 2 m below the ice surface. Both ocean temperature and salinity an increase trend over time, gradually from low temperature and low salt (-1.59±0.02°C and 33.30±0.02 psu on 16 April) to high temperature and high salt (-1.40±0.03°C and 33.39±0.02 psu on 23 April). These phenomena could be related to the weakening of tide vertical mixing during these periods.
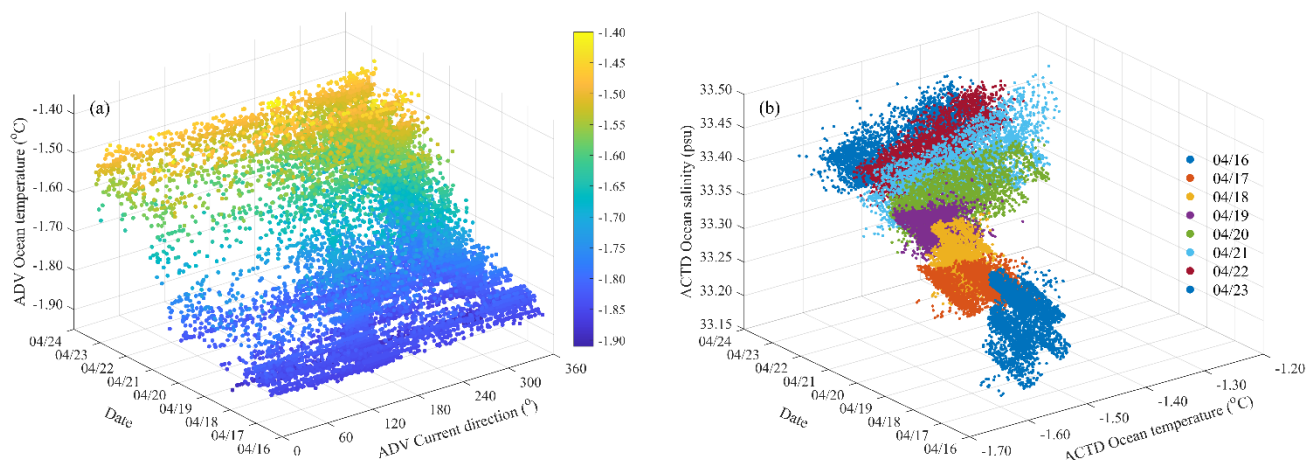
Figure 12. (a) The 3-D evolution of ocean velocity and direction at 5 m beneath landfast ice obtained by ADV; (b) The 3-D time-dependent distribution of ocean temperature and salinity obtained by ACTD at 2 m beneath landfast ice.

If assumed that there was no ocean temperature jump increase after the 20 April and it remained stable at -1.59℃, just as the average ocean temperature before 20 April, then the mean oceanic heat flux from 20 to 23 April would be 29.66±10.59 W m^{-2}, which was 33% smaller than the measured oceanic heat flux of 44.64±17.50 W m^{-2} during the same period. Landfast ice would froze more 0.36 cm at the bottom from 20 to 23 April if no ocean temperature jump increase, against to the 2 cm melt observed by SIMBA after 20 April. Therefore, tides transformation would influence the ocean current, temperature, and salinity beneath landfast ice and then oceanic heat flux, finally impacted the evolution of ice mass balance. The observations with high sampling frequency help to refine the oceanic heat flux variation at the sub-diurnal scale and better demonstrate the influence of tides on oceanic heat flux.

4.2 Comparisons with previous studies

Previous studies have estimated the oceanic heat flux under landfast ice in Antarctica with different methods and data intervals. Allison (1981) estimated oceanic heat flux near Mawson Station from monthly mean temperature and ice growth. At the early stage of sea ice growth, the thermohaline convection caused by the brine rejection makes the flux very high, could be as high as 50 W m^{-2}. Heil et al. (1996) used a multilayer thermodynamic model to simulate sea ice growth at Mawson Station. The multi-year averaged oceanic heat flux estimated by daily values was 7.9 W m^{-2}, and the annual mean was between 5 and 12 W m^{-2} from 1958 to 1986. Lei et al. (2010) estimated the oceanic heat flux using 30 minutes ice records in 2006, and the 5 day running mean oceanic heat flux in early April to be about 15–20 W m^{-2}. Yang et al. (2016) estimated the oceanic heat flux near Zhongshan Station by a thermodynamic model and the results was about 25 W m^{-2} in March and April. According to the weekly observation near Zhongshan Station, Zhao et al. (2019) interpolated and calculated the daily oceanic heat flux from March to May to be about 30.0 W m^{-2}. In this study, the averaged oceanic heat flux calculated by the residual energy method

and the bulk parameters method was based on a higher temporal resolution observation (2 minutes interval) and the results was about 32–34 W m^{-2} during the study (16 to 23 April), consistent with the previous studies.

5 Conclusions

The heat balance between atmosphere, ice, and ocean was one of the most important processes in the Polar Regions. The interaction at the atmosphere–ice interface has been well investigated, however the interaction at ice–ocean interface was rarely studied because of the limit of underwater observations. Oceanic boundary layer regimes beneath sea ice plays an important role on the growth and melting of sea ice. In this study, an integrated ice–ocean observation system including ADV, ACTD, and SIMBA were deployed near Zhongshan Station in Prydz Bay, East Antarctica. The minute-resolution ocean temperature, salinity, density, current, and heat flux were analysed and investigated in this paper for the first time in this region.

The 4.8 m long SIMBA temperature chain recorded vertical temperature profiles of air–snow–sea ice–ocean, which was used to estimate snow and ice thickness. The results show that landfast ice froze 2 cm at the bottom during 16–20 April, while melted by 2 cm during 21–23 April. ACTD recorded high frequency ocean temperature and salinity at 5 m depth beneath landfast ice. The mean ocean temperature showed a jump increase from -1.59±0.03℃ during 16–19 April to -1.47±0.07℃ during 20–23 April. The mean ocean salinity was 33.53±0.03 psu with an overall increasing trend of 0.013 psu day^{-1} during 16–23 April, while the growth rate was slowing down during 20–23 April, because the melting of ice bottom shut down the salt rejection related to ice freezing. The mean ocean density was 1026.84±0.02 kg m^{-3}, which increased slightly during the study period. The ocean current recorded by ADV showed that 34% of the current direction was northwest (300–330°) and the mean velocity was 3.13±1.63 cm s^{-1}, with a maximum up to 11.25 cm s^{-1} for 2 min time series and 10.23 cm s^{-1} for 1 hour mean time series.

The mean oceanic heat flux was estimated by the residual energy method and the bulk parameters method. The results showed a range of 7.64–97.88 W m^{-2} during the study period, with a mean of 34.95±17.52 W m^{-2} and 32.26±18.07 W m^{-2}, respectively for these two methods. Our results were consistent with previous studies, which usually was based on low frequency observations. The oceanic heat fluxes increased to twice after 20 April, which was related to the increase of ocean current velocity (from 2.68 cm s^{-1} to 3.65 cm s^{-1}) and the rise of ocean temperature (from -1.59 to -1.47℃). The increase of oceanic heat flux triggered basal melt and decrease the landfast ice thickness by 2 cm.

The tide transform from semi-diurnal to diurnal during the study period was possibly attribute to the significant rise of ocean temperature. From 16 to 23 April, the tidal amplitude weakened and the period of current variation became longer, which indicated that the ocean currents influenced by the coastal tide, played an important role on the ocean temperature, and then further affected the oceanic heat flux.

395

396 In this study, the high frequency of oceanic measurements provides us a chance to investigate the influences of oceanic regimes

397 beneath landfast ice in the diurnal scale. The bulk parameterization estimated the oceanic heat flux in more details than the

398 residual energy method. However, the analysis was limited to a short time in the initial stage of sea ice growth because of the

399 equipment malfunction. In future, we will carry out a longer field observation, to obtain a seasonal time series of ocean regimes

400 beneath landfast ice and further explore the detailed impact of oceanic heat flux on the growth of sea ice.

401

Data availability

403 Sea ice observed data are available upon request to the corresponding author.

404

Author contributions

406 JC conceptualized this study and designed the numerical methods. HH carried out the experiments and wrote the manuscript.

407 JC, PH and FH helped analyze the results and revised the manuscript. JM provided and helped process the sea ice observation

408 data. XC assisted during the writing progress and critically discussed the contents.

409

Competing interests

411 One of the co-authors is a member of the editorial board of *The Cryosphere*, and the authors also have no other competing

412 interests to declare.

413

Acknowledgement

415 This study is financially supported by the National Natural Science Foundation of China (41876212). PH was supported by

416 the Australian Government through Australian Antarctic Science projects 4506 and the International Space Science Institute

417 grant no. 406.

418

References

420 Allison, I.: Antarctic ice growth and oceanic heat flux, in Sea Level, Ice and Climate Change, Proceedings of the IUGG
421 Canberra Symposium, 1979, IAHS Publ., 131, 161–170, 1981.

422 Bigg, P. H.: Density of water in SI units over the range 0-40 C, Br. J. Appl. Phys., 18, 521–525, https://doi.org/10.1088/0508-
423 3443/18/4/315, 1967.

424 Clem, K. R., Fogt, R. L., Turner, J., Lintner, B. R., Marshall, G. J., Miller, J. R., and Renwick, J. A.: Record warming at the
425 South Pole during the past three decades, Nat. Clim. Chang., 10, 762–770, https://doi.org/10.1038/s41558-020-0815-z, 2020.

426 Comiso, J. C., Parkinson, C. L., Gersten, R., and Stock, L.: Accelerated decline in the Arctic sea ice cover, Geophys. Res. Lett.,
427 35, L01703, https://doi.org/10.1029/2007GL031972, 2008.

428 Fedotov, V. I., Cherepanov, N. V., and Tyshko, K. P.: Some Features of the Growth, Structure and Metamorphism of East
429 Antarctic Landfast Sea Ice, in: Antarctic Research Series, edited by: Jeffries, M. O., American Geophysical Union, Washington,
430 D. C., 343–354, https://doi.org/10.1029/AR074p0343, 2013.

431 Giles, K. A., Laxon, S. W., and Ridout, A. L.: Circumpolar thinning of Arctic sea ice following the 2007 record ice extent
432 minimum, Geophys. Res. Lett., 35, L22502, https://doi.org/10.1029/2008GL035710, 2008.

433 Guo, G., Shi, J., and Jiao, Y.: Temporal variability of vertical heat flux in the Makarov Basin during the ice camp observation
434 in summer 2010, Acta Oceanol. Sin., 34, 118–125, https://doi.org/10.1007/s13131-015-0755-z, 2015.

435 Heil, P.: Atmospheric conditions and fast ice at Davis, East Antarctica: A case study, J. Geophys. Res., 111, C05009,
436 https://doi.org/10.1029/2005JC002904, 2006.

437 Heil, P., Allison, I., and Lytle, V. I.: Seasonal and interannual variations of the oceanic heat flux under a landfast Antarctic sea
438 ice cover, J. Geophys. Res., 101, 25741–25752, https://doi.org/10.1029/96JC01921, 1996.

439 Kirillov, S., Dmitrenko, I., Babb, D., Rysgaard, S., and Barber, D.: The effect of ocean heat flux on seasonal ice growth in
440 Young Sound (Northeast Greenland): THE OCEAN HEAT FLUX IN YOUNG SOUND FJORD, J. Geophys. Res. Oceans,
441 120, 4803–4824, https://doi.org/10.1002/2015JC010720, 2015.

442 Lei, R., Li, Z., Cheng, B., Zhang, Z., and Heil, P.: Annual cycle of landfast sea ice in Prydz Bay, east Antarctica, J. Geophys.
443 Res., 115, C02006, https://doi.org/10.1029/2008JC005223, 2010.

444 Lei, R., Li, N., Heil, P., Cheng, B., Zhang, Z., and Sun, B.: Multiyear sea ice thermal regimes and oceanic heat flux derived
445 from an ice mass balance buoy in the Arctic Ocean: ARCTIC SEA-ICE THERMAL REGIMES, J. Geophys. Res. Oceans,
446 119, 537–547, https://doi.org/10.1002/2012JC008731, 2014.

447 Li, X., Shokr, M., Hui, F., Chi, Z., Heil, P., Chen, Z., Yu, Y., Zhai, M., and Cheng, X.: The spatio-temporal patterns of landfast
448 ice in Antarctica during 2006–2011 and 2016–2017 using high-resolution SAR imagery, Remote Sensing of Environment,
449 242, 111736, https://doi.org/10.1016/j.rse.2020.111736, 2020.

450 Liu, J. and Curry, J. A.: Accelerated warming of the Southern Ocean and its impacts on the hydrological cycle and sea ice,
451 Proceedings of the National Academy of Sciences, 107, 14987–14992, https://doi.org/10.1073/pnas.1003336107, 2010.

452 Manabe, S. and Stouffer, R. J.: Sensitivity of a global climate model to an increase of CO_2 concentration in the atmosphere,

453 J. Geophys. Res., 85, 5529, https://doi.org/10.1029/JC085iC10p05529, 1980.

454 Massom, R. A. and Stammerjohn, S. E.: Antarctic sea ice change and variability – Physical and ecological implications, Polar

455 Science, 4, 149–186, https://doi.org/10.1016/j.polar.2010.05.001, 2010.

456 Massom, R. A., Hill, K. L., Lytle, V. I., Worby, A. P., Paget, M. J., and Allison, I.: Effects of regional fast-ice and iceberg

457 distributions on the behaviour of the Mertz Glacier polynya, East Antarctica, Ann. Glaciol., 33, 391–398,

458 https://doi.org/10.3189/172756401781818518, 2001.

459 Maykut, G. A. and Untersteiner, N.: Some results from a time-dependent thermodynamic model of sea ice, J. Geophys. Res.,

460 76, 1550–1575, https://doi.org/10.1029/JC076i006p01550, 1971.

461 McPhee, M. G.: The Effect of the Oceanic Boundary Layer on the Mean Drift of Pack Ice: Application of a Simple Model, J.

462 Phys. Oceanogr., 9, 388–400, https://doi.org/10.1175/1520-0485(1979)009<0388:TEOTOB>2.0.CO;2, 1979.

463 McPhee, M. G.: Turbulent heat flux in the upper ocean under sea ice, J. Geophys. Res., 97, 5365,

464 https://doi.org/10.1029/92JC00239, 1992.

465 McPhee, M. G.: Turbulent stress at the ice/ocean interface and bottom surface hydraulic roughness during the SHEBA drift, J.

466 Geophys. Res., 107, 8037, https://doi.org/10.1029/2000JC000633, 2002.

467 McPhee, M. G. and Untersteiner, N.: Using sea ice to measure vertical heat flux in the ocean, J. Geophys. Res., 87, 2071,

468 https://doi.org/10.1029/JC087iC03p02071, 1982.

469 McPhee, M. G., Ackley, S. F., Guest, P., Stanton, T. P., Huber, B. A., Martinson, D. G., Morison, J. H., Muench, R. D., and

470 Padman, L.: The Antarctic Zone Flux Experiment, Bull. Amer. Meteor. Soc., 77, 1221–1232, https://doi.org/10.1175/1520-

471 0477(1996)077<1221:TAZFE>2.0.CO;2, 1996.

472 McPhee, M. G., Kottmeier, C., and Morison, J. H.: Ocean Heat Flux in the Central Weddell Sea during Winter, J. Phys.

473 Oceanogr., 29, 1166–1179, https://doi.org/10.1175/1520-0485(1999)029<1166:OHFITC>2.0.CO;2, 1999.

474 Miles, B. W. J., Stokes, C. R., and Jamieson, S. S. R.: Simultaneous disintegration of outlet glaciers in Porpoise Bay (Wilkes

475 Land), East Antarctica, driven by sea ice break-up, The Cryosphere, 11, 427–442, https://doi.org/10.5194/tc-11-427-2017,

476 2017.

477 Millero, F.: Freezing point of seawater, Eighth Report of the Joint Panel on Oceanographic Tables and Standards, 28, 29–31,

478 1978.

479 Millero, F. J. and Poisson, A.: International one-atmosphere equation of state of seawater, Deep Sea Research Part A.

480 Oceanographic Research Papers, 28, 625–629, https://doi.org/10.1016/0198-0149(81)90122-9, 1981.

481 Parkinson, C. L. and DiGirolamo, N. E.: Sea ice extents continue to set new records: Arctic, Antarctic, and global results,

482 Remote Sensing of Environment, 267, 112753, https://doi.org/10.1016/j.rse.2021.112753, 2021.

483 Parkinson, C. L. and Washington, W. M.: A large-scale numerical model of sea ice, J. Geophys. Res., 84, 311,

484 https://doi.org/10.1029/JC084iC01p00311, 1979.

485 Perovich, D. K. and Elder, B.: Estimates of ocean heat flux at SHEBA: ESTIMATES OF OCEAN HEAT FLUX AT SHEBA,

486 Geophys. Res. Lett., 29, 58-1-58–4, https://doi.org/10.1029/2001GL014171, 2002.

487 Raphael, M. N. and Handcock, M. S.: A new record minimum for Antarctic sea ice, Nat Rev Earth Environ, 3, 215–216,

488 https://doi.org/10.1038/s43017-022-00281-0, 2022.

489 Screen, J. A. and Simmonds, I.: The central role of diminishing sea ice in recent Arctic temperature amplification, Nature, 464,

490 1334–1337, https://doi.org/10.1038/nature09051, 2010.

491 Semtner, A. J.: A Model for the Thermodynamic Growth of Sea Ice in Numerical Investigations of Climate, J. Phys. Oceanogr.,

492 6, 379–389, https://doi.org/10.1175/1520-0485(1976)006<0379:AMFTTG>2.0.CO;2, 1976.

493 Untersteiner, N.: On the mass and heat budget of arctic sea ice, Arch. Met. Geoph. Biokl. A., 12, 151–182,

494 https://doi.org/10.1007/BF02247491, 1961.

495 Wang, J., Luo, H., Yang, Q., Liu, J., Yu, L., Shi, Q., and Han, B.: An Unprecedented Record Low Antarctic Sea-ice Extent

496 during Austral Summer 2022, Adv. Atmos. Sci., s00376-022-2087–1, https://doi.org/10.1007/s00376-022-2087-1, 2022.

497 Yang, Y., Zhijun, L., Leppäranta, M., Cheng, B., Shi, L., and Lei, R.: Modelling the thickness of landfast sea ice in Prydz Bay,

498 East Antarctica, Antarctic Science, 28, 59–70, https://doi.org/10.1017/S0954102015000449, 2016.

499 Zhao, J., Yang, Q., Cheng, B., Leppäranta, M., Hui, F., Xie, S., Chen, M., Yu, Y., Tian, Z., Li, M., and Zhang, L.: Spatial and

500 temporal evolution of landfast ice near Zhongshan Station, East Antarctica, over an annual cycle in 2011/2012, Acta Oceanol.

501 Sin., 38, 51–61, https://doi.org/10.1007/s13131-018-1339-5, 2019.

502